PHYSICAL REVIEW B **77**, 174407 (2008)

Magnetization reversal of microstructured kagome lattices

A. Westphalen, A. Schumann, A. Remhof, and H. Zabel*
Institut für Experimentalphysik/Festkörperphysik, Ruhr-Universität Bochum, 44780 Bochum, Germany

M. Karolak, B. Baxevanis, and E. Y. Vedmedenko
Institut für Angewandte Physik, Universität Hamburg, 20355 Hamburg, Germany

T. Last and U. Kunze
Institut für Werkstoffe und Nanoelektronik, Ruhr-Universität Bochum, 44780 Bochum, Germany

T. Eimüller
Nachwuchsgruppe Magnetische Mikroskopie, Ruhr-Universität Bochum, 44780 Bochum, Germany
(Received 1 November 2007; revised manuscript received 2 April 2008; published 5 May 2008)

We report on a magneto-optical Kerr effect (MOKE) investigation of microstructured rectangular islands, which have been arranged on kagome lattices. The magnetization reversal was studied by regular longitudinal vector MOKE in specular geometry as well as in Bragg MOKE geometry, using the diffraction spots from the grating for hysteresis measurements. The magnetization at remanence is imaged by using magnetic force microscopy and x-ray photoemission electron microscopy. The measurements have been compared to the results of micromagnetic simulations, which allow a detailed interpretation of the experimental data. It is demonstrated that the magnetization reversal process in an external magnetic field strongly depends on the shape and the interparticle spacing between the islands. For the thorough understanding of the nontrivial dependence of magnetization reversal on the array geometry, the magnetic moments of the islands and the energy barriers for magnetization switching in individual elements have been theoretically analyzed. The performed analysis provides insight into the magnetostatic interactions and probability of switching paths taken by the particles arranged on lattices with kagome symmetry during the magnetization reversal process.

DOI: 10.1103/PhysRevB.77.174407 PACS number(s): 75.60.Jk, 78.20.Ls, 75.70.Cn, 07.05.Tp

I. INTRODUCTION

Kagome lattices have become the paradigm for the investigation of lattice structures with geometrical spin frustration. The term *kagome* refers to a Japanese bamboo basket (kago) with a woven pattern (me) that is composed of interlaced triangles. The number of nearest neighbors of a lattice point is 4 as on a square lattice; however, the angles between the connecting lines to the nearest neighbors on the triangular lattice are 60° instead of 90°.

Kagome-type ordering has been investigated in $SrCr_{8-x}Ga_{4+x}O_{19}$ and in the jarosite family compounds,[1–4] e.g., the Heisenberg kagome lattice antiferromagnet $KFe_3(OH)_6(SO_4)_2$.[5–7] Kagome has also been reported for ^{3}He on graphite and some molecular magnets.[8,9]

Using patterning methods of periodic arrays, magnetic ordering and frustration can be investigated for different symmetries on mesoscopic length scales. For instance, magnetic islands with dipolar stray fields can be placed on regular grids, such as square or triangular lattices. While a large number of studies have reported on the magnetic state of individual magnetic nanoparticles and their reversal process (see, for a review, Ref. 10), few studies have specifically investigated the interaction between magnetic particles. Cowburn has studied the antiferromagnetic interaction between strings of magnetic dipoles;[11] magnetic interactions within patterned cobalt nanostructures were investigated by Dunin-Borkowski *et al.*;[12] the interdot magnetostatic interaction and its effect on the magnetization reversal in circular dot arrays was considered by Novosad *et al.*[13] Wang *et al.* have studied geometrically frustrated arrays of nanoscale ferromagnetic islands on a square lattice, which can be described by the ice rules.[14] In a similar study, Remhof *et al.* have investigated the geometrical frustration on a square lattice with varying dipolar interaction.[15] In contrast to the work of Wang *et al.*, Remhof *et al.* dominantly observe the onion state. Only at large distances, a so-called horseshoe state can be recognized coexisting with the onion state. The obtained configuration is very different from that of the dipolar kagome spin ice reported by Tabata *et al.*[16]

Fraerman and Sapozhnikov theoretically considered the interaction of two-dimensional magnetic nanoparticles on regular lattices, and they have provided analytical expressions for the magnetic hysteresis curve of a system with interaction, where it is shown that during a magnetization reversal, the system undergoes a number of metastable states.[17] Numerical calculations of the interplay between magnetocrystalline anisotropy and dipolar stray fields for a square dot array were published by Takagi and Ploog[18] and Suess *et al.*[19] Vedmedenko *et al.* showed that the interparticle distances in arrays strongly affect the magnetostatic interactions and control their collective behavior.[20]

Here, we report on the geometric frustration of magnetic moments arranged on a kagome lattice. The kagome lattice intrinsically exhibits a sixfold symmetry. The interest does not only lie in the collective remanent state of rectangular bars arranged in a kagome structure but also in the magnetic reversal process. Remagnetization processes are complex

even for easy geometrical configurations.[21] The aim of this paper is to report on studies of the reversal in different kagome structures. Varying the size of the rectangular bars and the interparticle distance the effect of stray field interaction on the magnetization reversal was investigated by using magneto-optical Kerr effect (MOKE) in the vector MOKE[22] and in the Bragg MOKE configuration,[23] as well as by magnetic force microscopy (MFM) and x-ray photoemission electron microscopy (X-PEEM) in real space. We have combined MOKE measurements with micromagnetic simulations for the analysis of the magnetization reversal and show that magnetic hysteresis measurements can be reproduced very well by the simulations. By calculating the magnetic moments and estimating the energy barriers for magnetization switching in individual elements, the different paths for the magnetization reversal in arrays with kagome symmetry can be rationalized.

This paper is organized as follows. In Sec. II we describe the sample preparation, the conditions for the MOKE experiments, and the micromagnetic simulations. Section III is divided into two subsections: in the first subsection, the reversal process is discussed for the magnetic field applied parallel to one of the sublattices (0° orientation), and in the second subsection, the results are reported for the magnetic field applied perpendicular to one of the sublattices (30° orientation). In Sec. IV, we present an analysis of the effect of higher multipolar moments on the collective magnetic ordering in an array, and we provide energy landscapes for different magnetization reversal paths.

II. EXPERIMENTAL DETAILS

A. Sample preparation

A polycrystalline Fe film with a thickness of $t=20$ nm was deposited on a silicon (100) substrate at room temperature. After spin coating with negative resist, templates of the kagome structures were fabricated in 800×800 μm^2 fields by e-beam lithography using a FEI Quanta 200FEG scanning electron microscope equipped with Raith ELPHY QUANTUM software. Four different arrays of rectangular Fe islands with lateral dimensions $l\times w$ of 3.8×0.3, 4.7×0.3, 2.7×0.15, and 2.7×0.15 μm^2 are set in kagome grids with heights h of 9.7, 9.7, 6.5, and 5.6 μm, respectively (see Fig. 1 and Table I). According to Table I, we will denote the kagome lattices as $K1$, $K2$, $K3$, and $K4$. The transformation of the patterns from the resist into the Fe film was done by ion beam etching in ultrahigh vacuum conditions. The resulting patterns were imaged by using scanning electron microscopy (SEM), atomic force microscopy, and MFM. A representative SEM image of kagome lattice $K1$ is shown in Fig. 1. Kagome lattices can be separated into three sublattices. Each sublattice consists of a chain of rectangular bars. The chains are rotated 60° against each other. In the following, we will denote these sublattices as $S1$, $S2$, and $S3$ (see Fig. 1).

The polycrystallinity of the Fe film is advantageous because it suppresses the magneto-crystalline anisotropy while keeping the shape anisotropy determined by the aspect ratio of the particles. The rectangular shape causes the easy axis to be parallel to the long side of the particle. Choosing Fe as the material for the rectangular islands, we expect domain formation during the magnetization reversal. As will be explained in the next sections, the Bragg MOKE technique is very sensitive to domain formation. Thus, domain formation will not escape our attention.

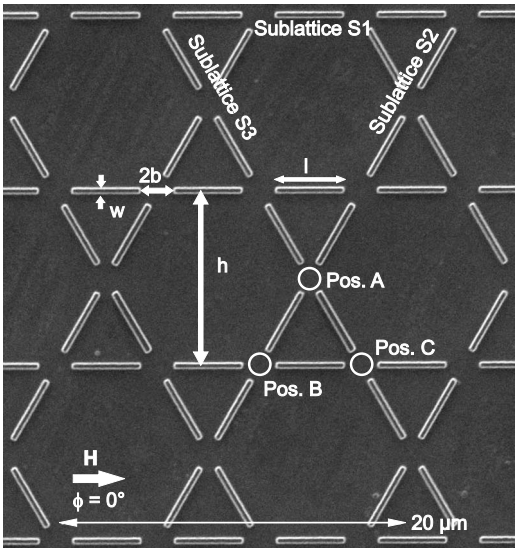

FIG. 1. Scanning electron micrograph image of rectangular Fe islands placed between the nodes of kagome lattice $K1$. The lateral dimensions of the islands are $l=3.8$ μm and $w=0.3$ μm, the height is $h=9.7$ μm, and the interparticle distance is $b=1.9$ μm. The kagome lattice can be separated into three sublattices, $S1$, $S2$, and $S3$, each of them consisting of a chain of rectangular islands. In the center of the marked positions, A, B, and C, the value of the stray field H_{stray} is obtained from micromagnetic simulations. For further details, we refer to the text.

B. Magneto-optical Kerr effect setup and magnetic force microscopy

For the magnetic characterization, we used the longitudinal Kerr effect with s-polarized light from a HeNe laser (wavelength $\lambda=632.8$ nm) and a high-resolution polarization detection unit, as described in Refs. 24 and 25.

The measured Kerr angle θ_x is proportional to the component of the magnetization vector **M** projected into the plane of incidence, $\theta_x \propto m_x$. To determine the complete magnetization vector, we also performed MOKE measurements with the sample and the external magnetic field rotated by 90°,

TABLE I. Size of the kagome lattices and lateral dimensions of the rectangular islands. For further explanation, we refer to Fig. 1 and to the text.

Lattice	h (μm)	l (μm)	w (μm)	b (μm)
$K1$	9.7	3.8	0.3	1.9
$K2$	9.7	4.7	0.3	1.0
$K3$	6.5	2.7	0.15	1.1
$K4$	5.6	2.7	0.15	0.65

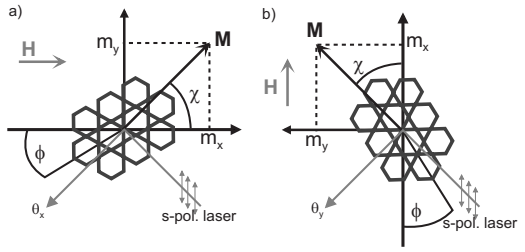

FIG. 2. Sketch of the vector MOKE configuration to measure the Kerr rotation of (a) the x component θ_x and (b) the y component θ_y.

such that the angle χ between the orientation of the structure and the field is kept constant, but the magnetization component m_y is in the plane of incidence. In this configuration, longitudinal MOKE detects the magnetization component parallel to the plane of incidence but perpendicular to the applied field, $\theta_y \propto m_y$ (Refs. 23 and 26) (see Fig. 2). Both components of the magnetization vector $\mathbf{M}$, m_x and m_y, yield the vector sum of the average magnetization vector $\langle \mathbf{M} \rangle$, as measured within the region illuminated by the laser spot. The distinction between the orientation of the applied field and the component of the magnetization being observed is of fundamental importance for the so-called vector MOKE technique. Both in-plane components of the magnetization vector are measured via Kerr rotation. Otherwise, using normal longitudinal MOKE for the x component and transversal MOKE for the y component, both components cannot be combined to the whole magnetization vector because of the unknown proportionality between magnetization and Kerr rotation or intensity change, respectively. Another advantage of the vector MOKE technique is that the experimental setup does not have to be changed for measuring both magnetization components. We used a quadrupole magnet, which allows easy rotation of the external field by 90°, while the sample was rotated by a stepping motor.

In addition to vector MOKE, we performed Bragg MOKE measurements at the reciprocal lattice points of the kagome lattice and then again determined the m_x and m_y components of the magnetization vector. All Bragg MOKE measurements were recorded in the scattering plane defined by the incident beam and the normal to the film.

As discussed in Ref. 27, the magneto-optical contribution to the nth order diffracted beam is proportional to the magnetic form factor f_n^m defined by

$$f^n(m_{x(y)}) = \int m_{x(y)} \exp(in\ \mathbf{G} \cdot \mathbf{r}) dS, \tag{1}$$

where $\mathbf{G}$ is the reciprocal lattice vector, $m_{x(y)}$ is the component of the magnetization under investigation, and the integral is carried out over a unit cell of the structure. The magnetization normalized to the saturation can be written in the form

$$M^n_{x(y)} \propto \Re[f^n(m_{x(y)})] + A_n \Im[(f^n(m_{x(y)})\ ]. \tag{2}$$

Here, A_n has been treated as an adjustable parameter. Unlike the vector MOKE results, the Bragg MOKE hysteresis curves have no straight forward and easy interpretation. Similar to optical and x-ray diffraction, the nth order diffraction spot represents the nth order Fourier transform of the magnetic form factor. We have recently extended the Bragg MOKE method such that vector MOKE can be combined with Bragg MOKE, which allows determining the complete magnetization vector at the nth order of diffraction.[28] This has the advantage that only the periodic part of the MOKE signal is filtered out from all other effects, which may contribute to the total MOKE signal. However, for the present study, we have to include a term for second-order contributions in order to reproduce the hysteresis loops of the y component. It is known that for thin Fe films, second-order magneto-optic effects can play a decisive role.[28–31] In this case, we write the Kerr angle for the y component in the form

$$\theta_y^n \propto M_y^n + \alpha M_x^n M_y^n, \tag{3}$$

where M_x^n and M_y^n are obtained from the simulations by using Eqs. (1) and (2), where α is a phenomenological parameter. With the additional term, we can reproduce the shape of the measured hysteresis loops from micromagnetic simulations. The x component is less affected by higher order effects, but in some cases, they are not completely negligible, as we will see in the specular hysteresis loop of $K2$. It should be kept in mind that the physics behind second-order effects in MOKE is complex. Here, the parameter α is used as a fitting parameter.

Real space images of the magnetization distribution at remanence have been taken with MFM, using a Digital Instrument Nanoscope IIIa microscope. The pyramidal tip probing the sample consists of etched silicon coated with Co/Cr.

Furthermore, images were taken for some samples with a x-ray photoemission electron microscope at the Advanced Light Source of the Lawrence Berkeley National Laboratory in Berkeley, USA. The instrument PEEM II of beamline 7 was used for magnetic imaging based on x-ray magnetic circular dichroism.

C. Procedures for experiments and simulations

We have measured hysteresis loops at the specular and the first three diffraction spots in the scattering plane both for the x and y components and for two different sample orientations with respect to the applied magnetic field direction. The orientation $\phi=0°$ refers to an external magnetic field applied parallel to sublattice $S1$ (see Fig. 1), which is the easy axis for this sublattice. The orientation $\phi=30°$ refers to a field direction perpendicular to sublattice $S2$, i.e., the field is applied parallel to the hard axis of the elements in sublattice $S2$.

In order to understand the remagnetization process and to interpret the measured hysteresis loops, we combined vector with Bragg MOKE and performed micromagnetic simulations, using the object oriented micromagnetic framework (OOMMF 1.2A3).[32] The material parameters for Fe tabulated in the OOMMF program were used (exchange stiffness $A=21 \times 10^{-12}$ J/m and saturation magnetization $M_s=1700$

$\times 10^3$ A/m). As the rectangular islands are polycrystalline, we have set the anisotropy constant to $K_1=0$. For simplicity and optimization of the computational time, we concentrate on sections of the kagome lattices containing 12 hexagons. The cell size varies depending on the size of the section under investigation. We chose a cell size of 100 nm for lattices $K1$ and $K2$, 67 nm for $K4$, and 50 nm for $K3$. Thus, a section consists of a maximum of 300 000 cells. This compromise was necessary in order to preserve reasonable computation time. A cell size of 100 nm is rather big for obtaining information on a detailed domain structure inside a single rectangular island. However, we are interested in the magnetization reversal of the rectangular islands and the different magnetic configurations in the kagome structures. The comparison of the measured data with the simulations show that the rather rough cell size is not a severe disadvantage and that we are able to reproduce the measured hysteresis loops. We have also tested smaller cell sizes in order to focus on the structure of the end domains in the islands and noted that the global magnetic configurations are not affected by the choice of the cell size. This will be discussed in more detail later for the sample orientation of $\phi=30°$. We also extracted the value of the stray field H_{stray} at three different vertices A, B, and C of the kagome lattices marked in Fig. 1. These positions are geometrically equivalent, but the stray fields depend on the number of moments pointing into a vertex, as compared to those pointing out, and whether the moments of same polarity are nearest neighbors or opposite to each other. The stray field is important for the discussion of correlation and frustration in the kagome lattices.

In addition, we have calculated the higher order magnetic moments of the particles in the kagome lattice and we have estimated energy barriers for the magnetization switching in individual elements. Furthermore, we have analyzed the magnetostatic interactions in the kagome ensembles for different states as well as the energy barriers for the magnetization reversal. This will be described in detail in Sec. IV.

In the following section, we will only present the data obtained at the specular and first diffraction spots. The measurements and simulations of the hysteresis curves at the second and third diffraction spots do not contain additional information. Therefore, we used them only to control the accuracy of the simulations.

III. EXPERIMENTAL RESULTS

A. Sample orientation $\phi=0°$

1. Specular magneto-optical Kerr effect results

Figure 3 shows the Kerr hysteresis loops for all four lattices, $K1-K4$, measured at the specular spot and in normal longitudinal geometry, i.e., the x component of the average magnetization with the field applied parallel to sublattice $S1$. The inset reproduces the magnetization loop of the unpatterned Fe film.

The main differences between the patterned and the unpatterned film are the sign of the nucleation field H_N, the magnitude of the coercive field, and the squareness of the hysteresis. For the unpatterned film, the nucleation field is positive, the coercive field is small, and the hysteresis is squared, in agreement with values for polycrystalline Fe films reported in the literature.[22] In contrast, after patterning, the nucleation field is negative, the coercive field is enhanced, and the magnetization loops are rounded, containing in some cases steps that were not present before. The nucleation fields and the coercive fields of the homogenous film and the kagome lattices are listed in Table II. The nucleation field was evaluated as the first deviation from the horizontal line, where the emphasis is on the tendency, not on the precise value, which would be difficult to obtain. The negative nucleation field is due to the rotation of the magnetization in the sublattices $S2$ and $S3$ toward the easy axis, as the field decreases from negative saturation. Rotation implies an increase of the m_y component and, thus, a decrease of the m_x component measured in the longitudinal setup.

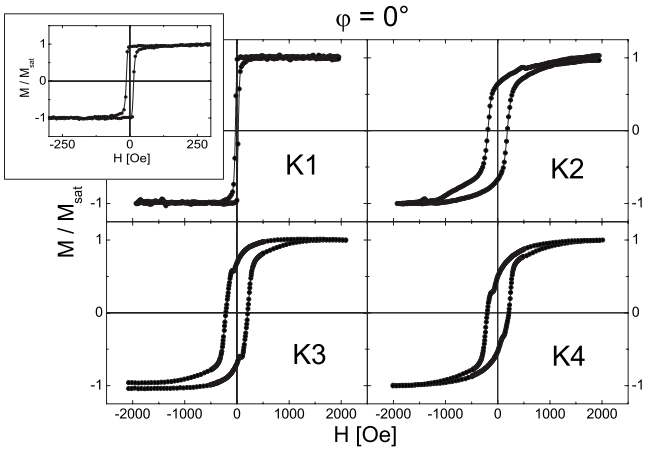

FIG. 3. Specular MOKE hysteresis loops showing the x component of the four different kagome lattices in the orientation $\phi=0°$.

The hysteresis loop of lattice $K1$ with the largest distance b between the bars is quite similar to the one of the homogeneous film. There is only a slight increase in the coercive field from 14 to 30 Oe. With decreasing distance b, the coercivity of lattices $K2-K4$ drastically increases.

The hysteresis loop of $K2$ is asymmetric. This is an indication of the second-order contributions to the Kerr signal mentioned before. In the hysteresis loops of $K3$ and $K4$, a step occurs at $H=80$ and 110 Oe, respectively. The step is more pronounced for lattice $K3$ than for lattice $K4$. We will discuss this behavior in the next paragraphs and we will ana-

TABLE II. Nucleation field H_N and coercive field H_c obtained from the specular MOKE hysteresis curves shown in Fig. 3 for $\phi=0°$.

Lattice	H_N (Oe)	H_c (Oe)
$K1$	−40	30
$K2$	−1000	185
$K3$	−500	209
$K4$	−1000	207
Homogeneous film	10	14

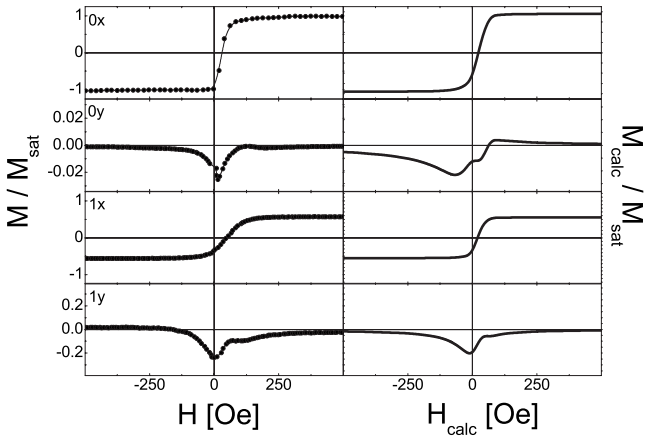

FIG. 4. Kagome lattice $K1$: Measured (left panel) and calculated Bragg MOKE hysteresis loops (right panel) for the x and y components at the diffraction spots for $\phi=0°$; only the ascending branches of the hysteresis loops are shown.

lyze the results of the simulated magnetization profiles. In the following plots of the measured and calculated hysteresis curves, we will only show the ascending branches of the loops for clarity.

2. Vector magneto-optical Kerr effect results, K1

In Fig. 4, the experimental vector MOKE results taken at the specular and first diffraction spots are reproduced in the left panels and compared in the right panels with the OOMMF simulation of the MOKE signal. Corresponding real space pictures of the magnetization distribution in the K_1 lattice are shown in Fig. 5 for two field values. Coming from negative saturation to remanence ($H_{calc}=0$ Oe) in the simulation of kagome lattice $K1$, the magnetization rotates inside the rectangular bars such that the magnetization vectors lie parallel to the long side of the rectangles, i.e., the magnetization points in the easy axis direction of each sublattice (see Fig. 5, the arrows are a guide to the eyes and indicate the magnetization direction). The rotation process is strongly reflected in the m_y component of the experimental Bragg MOKE curves,

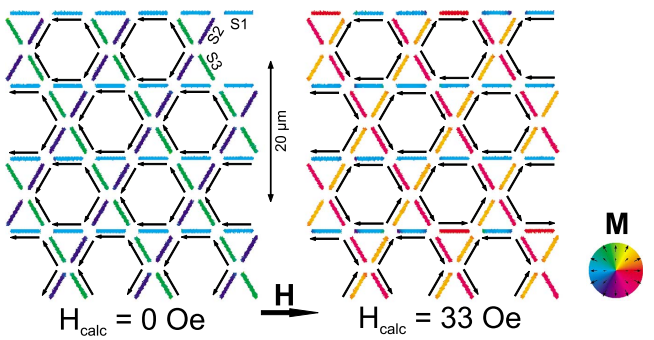

FIG. 5. (Color online) Kagome lattice $K1$: Calculated magnetization distribution in the three sublattices $S1$, $S2$, and $S3$. The left panel is calculated for an external field $H_{calc}=0$, the right panel for a field $H_{calc}=33$ Oe oriented parallel to the sublattice $S1$, which is referred to as the orientation $\phi=0°$. The arrows indicate the net magnetization direction inside the rectangular islands.

which culminates in a peak around $H=0$ Oe. This peak can be reproduced in the simulated hysteresis of the m_y component ($0y$ and $1y$ in Fig. 4). The remanent state can be characterized as an *onion* state. The term *onion* state usually refers to a domain structure observed in closed magnetic rings with two magnetization directions opposing each other and resulting in two domain walls.[33] In this context, we use the term onion state in a generalized fashion, referring to the number of opposing dipole pairs (two in this case) in one particular ring. In this state, all three sublattices have parallel or ferromagnetic alignment. In the ideal case, the magnetization component m_y should be zero at remanence. The measured hysteresis curves $0y$ for $K1-K4$ show a magnetization value normalized to the saturation of $m_y \approx 0.05$. In the micromagnetic simulations, a value of $m_y \approx 0.003$ is calculated (data not shown here). As mentioned above, higher order effects have to be taken into account in the MOKE signal. By using Eq. (3), the simulated hysteresis curves are fit to the measured ones. Thus, the nonzero value in the component m_y for $0y$ is a higher order effect of the measurement method.

Increasing the magnetic field in the next computational step leads to a completely different magnetization distribution. At $H_{calc}=33$ Oe, the magnetization in all particles of sublattices $S2$ and $S3$ has reversed its direction, but only a few bars in sublattice $S1$ have switched. This leads to a closed magnetic flux configuration in each triangle of the kagome lattice with only a few defects. In the next computational step, at $H_{calc}=66$ Oe, all bars of sublattice $S1$ reverse (magnetization profile not shown). The calculated curve $0y$ shows a peak at $H_{calc}=66$ Oe, and the corresponding peak in the experimental curve occurs at $H=120$ Oe. After the reversal of $S1$, the kagome lattice is in a reversed onion state. Increasing the magnetic field further forces the magnetization in sublattices $S2$ and $S3$ to rotate into the positive field direction. The intermediate state between the left- and right-oriented onion state is a remarkable and highly symmetric state, with ferromagnetic alignment of the bars in each sublattice. The switching between the left- and right-oriented onion states will be discussed in more detail in Sec. IV.

3. Vector magneto-optical Kerr effect results, K2

As the distance b between the bars is reduced from $K1$ to $K2$, the magnetic coupling between the bars becomes stronger. This leads to a completely different magnetization reversal than observed in $K1$. The experimental and simulated MOKE results are shown in Fig. 6; some real space maps of the magnetization distribution are reproduced in Fig. 7. Up to remanence, the calculated magnetization profiles show a similar behavior as in $K1$: the magnetization rotates inside the bars toward the easy axis direction and forms an onion state. In the next computational step, which is depicted in Fig. 7 ($H_{calc}=33$ Oe), the magnetization is first reversed in the bars of sublattice $S1$, whereas sublattices $S2$ and $S3$ remain or show some domain formation. In this state again, closed flux triangles are formed, however, now, by switching of $S1$ instead of $S2$ and $S3$. In the calculated Bragg MOKE curves, a strong peak occurs in $0y$ and a step in $1y$, which is more pronounced here than in the measured curves (see Fig. 6). The reversal of sublattice $S1$ takes place in a more narrow

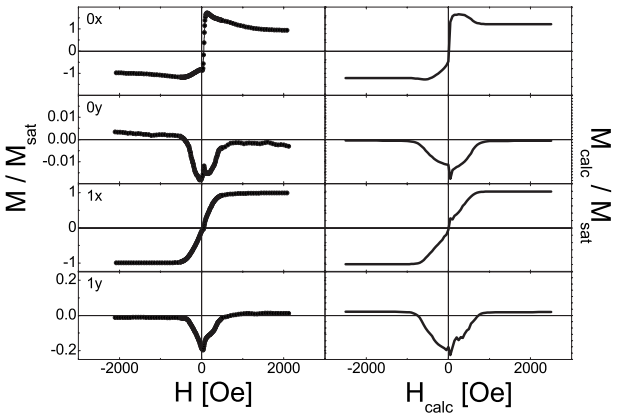

FIG. 6. Measured (left panel) and calculated Bragg MOKE hysteresis loops (right panel) as in Fig. 4 but for kagome lattice *K*2.

field region than in lattice *K*1. This is due to the higher stray field H_{stray} between the rectangular bars, especially at positions *B* and *C* (see Table III). At H_{calc}=166 Oe, in most of the domains, the magnetization reverses and points along the easy direction or is slightly tilted to the positive field direction. During this process, the measured hysteresis data show a peak in 0*y*, 1*x*, and 1*y* at *H*=100 Oe, which is reproduced in the calculated data at H_{calc}=166 Oe. A further increase in the magnetic field leads to a rotation of the magnetization in sublattices *S*2 and *S*3 into the positive field direction.

4. Vector magneto-optical Kerr effect results, K3 and K4

The magnetization reversals in *K*3 and *K*4 are similar to the one in *K*2, as can be seen by the MOKE hysteresis loops in Figs. 8 and 9. Like in lattice *K*2, the magnetization switches first in sublattice *S*1 followed by a switching in sublattices *S*2 and *S*3. However, the switching fields change. The reversal process for sublattice *S*1 lasts from H_{calc}=0 to 133 Oe in lattice *K*3 and from H_{calc}=33 to 66 Oe in lattice *K*4. The magnetization profiles show that initially, only a few rectangular bars switch their magnetization from negative to positive direction (see Figs. 10 and 11). The first domains in sublattices *S*2 and *S*3 appear at H_{calc}=66 Oe in both kagome lattices. The magnetic field has to be increased to H_{calc}=300 Oe for *K*3 and to 333 Oe for *K*4 before all

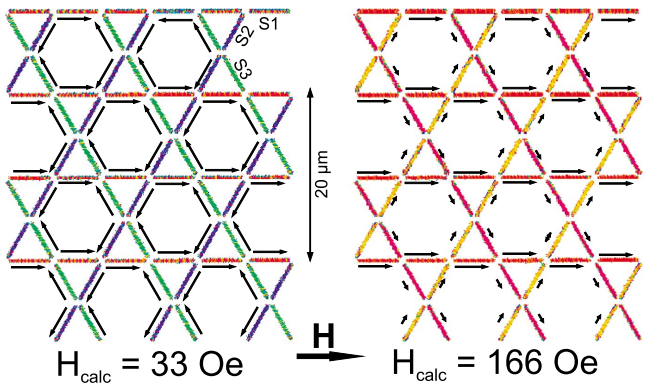

FIG. 7. (Color online) Calculated magnetization distribution for kagome lattice *K*2. For further details, see Fig. 5.

TABLE III. Stray field H_{stray} obtained from the micromagnetic simulations in remanence for ϕ=0°. For further explanation, we refer to the text.

Lattice	b (μm)	H_{stray} (Oe) Position *A*	Position *B*	Position *C*
*K*1	1.9	20	40	40
*K*2	1.0	96	166	179
*K*3	1.1	50	84	78
*K*4	0.65	120	166	168

particles in the sublattices *S*2 and *S*3 have reversed their magnetization. The higher reversal field for *K*4 is due the fact that the stray field H_{stray} is larger in lattice *K*4 than in *K*3 (see Table III) because of the smaller distance *b* of the bars. As sublattices *S*2 and *S*3 are oriented more toward a hard axis direction than toward an easy axis direction, the remagnetization process lasts longer in *K*4 than in *K*3.

5. Sublattice hysteresis curves

In order to explain the steps that occur in the experimental hysteresis loops 0*x* in *K*3 and *K*4, we have separately calculated the hysteresis curves 0*x* of the different sublattices. In Fig. 12, the hysteresis curves of the sublattices and of the whole structure are depicted. As discussed before, sublattices *S*2 and *S*3 similarly behave; the hysteresis curves of these sublattices are equal. For *K*1, the coercive field of sublattice *S*1 is larger than for *S*2 and *S*3 in agreement with the switching of *S*2 and *S*3 before the magnetization reverses in *S*1. In *K*2–*K*4, the opposite case occurs. Now, the origin of the step becomes clear. The hysteresis curves of *K*1 do not show a step because the switching of *S*1 starts while the magnetization reversal in *S*2 and *S*3 has not yet finished. In *K*2, a similar process occurs, but in a reversed sequence. However, in *K*3 and *K*4, the switching process in *S*2 and *S*3 takes place in a field region where the reversal process has already finished in *S*1. Thus, a step in the hysteresis becomes visible.

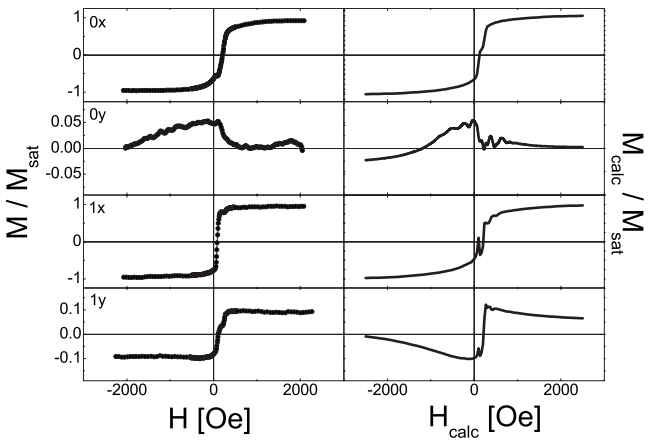

FIG. 8. Measured (left panel) and calculated Bragg MOKE hysteresis loops (right panel) as in Fig. 4 but for kagome lattice *K*3.

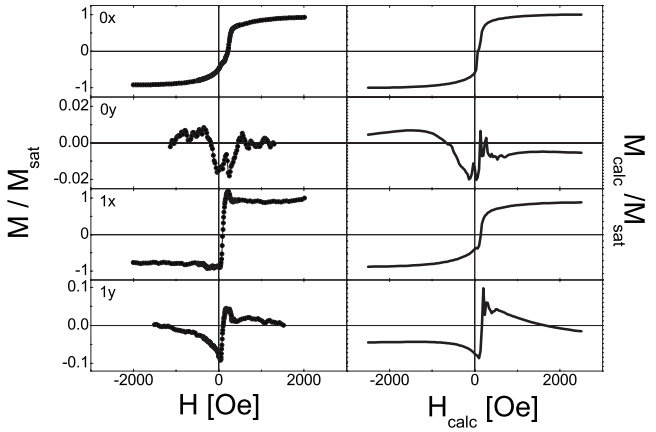

FIG. 9. Measured (left panel) and calculated Bragg MOKE hysteresis loops (right panel) as in Fig. 4 but for kagome lattice $K4$.

6. Magnetic force microscopy images

To confirm the reliability of the simulated magnetization profiles, we recorded MFM images at remanence. In Fig. 13, a MFM image of the kagome lattice $K4$ is depicted for the orientation $\phi=0°$. Each individual bar represents a magnetic moment; no domain formation within single bars could be observed. At remanence, the magnetic orientation of the ferromagnetic bars is parallel within each sublattice, confirming the onion state. MFM images of the other three kagome lattices show the same behavior (data not shown here); the results are in very good agreement with the simulated magnetization profiles.

7. Stray fields for the $\phi=0°$ orientation

Decreasing the size of the kagome lattice leads to an increasing value for the saturation field H_{sat} and the magnetizaton reversal process extends over an increasing magnetic field region. The distance b between the rectangular bars has a strong effect on the stray field H_{stray} at vertices A, B, and C. The stray field is always smaller at position A than at positions B and C because at the latter positions, sublattice $S1$ has its magnetic easy direction aligned parallel to the external field. This leads to an effective coupling between the rectangular bars and thus to a higher stray field value than at position A, where the stray fields of opposing dipoles partly

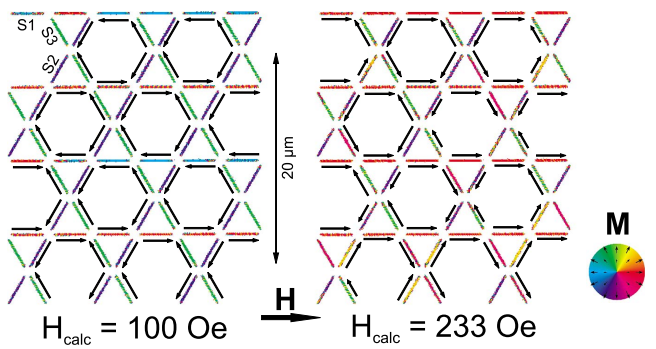

FIG. 10. (Color online) Calculated magnetization distribution for kagome lattice $K3$. For further details, see Fig. 5.

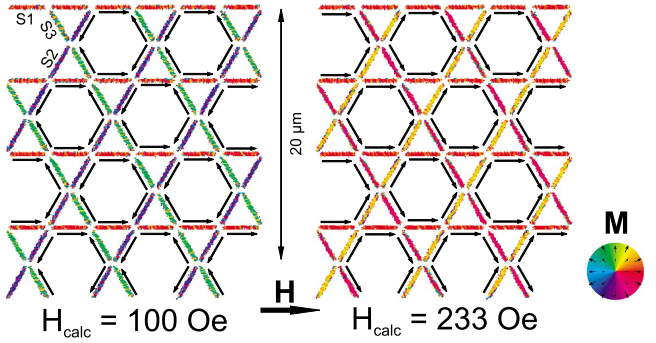

FIG. 11. (Color online) Calculated magnetization distribution for kagome lattice $K4$. For further details, see Fig. 5.

compensate. For symmetry reasons, the strength of the demagnetizing field at positions B and C is identical. This is also seen in the MFM image, which shows more contrast for vertices B and C than for A.

B. Sample orientation $\phi=30°$

In this paragraph, we report on the magnetization reversal process for the sample orientation $\phi=30°$. The diffraction spots of the sample allow a precise orientation of the kagome lattices; thus, the external field is perpendicularly applied to the rectangles of sublattice $S2$, i.e., sublattice $S2$ is oriented in the hard axis direction, while for sublattices $S1$ and $S3$, the field direction and the easy axes include an angle of 15°. This implies that, now, vertices A and B are degenerate with respect to their stray field, while vertex C is different. We expect that at remanence after saturation in a negative field, the magnetization vectors in $S1$ and $S3$ are relaxed to their easy axes, while $S2$ is frustrated. Depending on the strength of the interaction, $S2$ may either be oriented up or down with a 50% probability or may break up into domains. Which scenario will actually occur can be seen in the kagome lattices $K1-K4$, featuring different particle spacings b.

1. Vector magneto-optical Kerr effect results, K1

In Fig. 14, the Kerr hysteresis curves of lattice $K1$ are depicted. The measurements at the specular spot ($0x$ and $0y$)

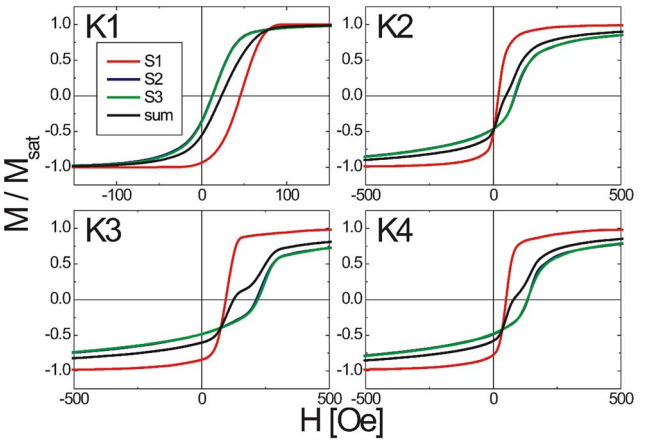

FIG. 12. (Color online) Hysteresis loops $0x$ of each sublattice $S1$ (red), $S2$ (blue), and $S3$ (green) obtained from the simulations of the four kagome structures. The black line corresponds to the sum hysteresis loop.

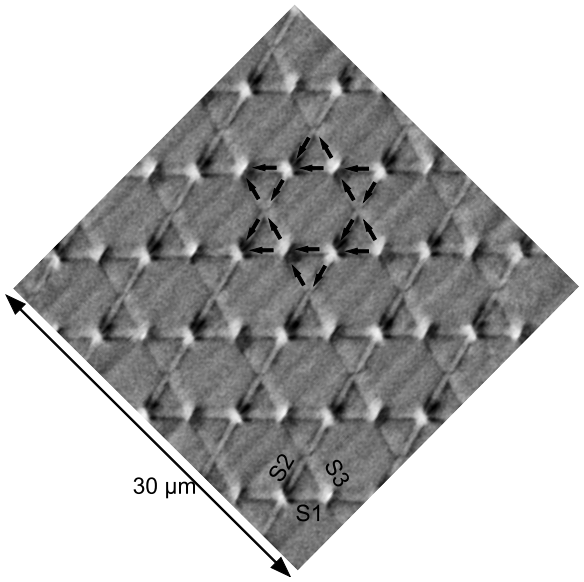

FIG. 13. Magnetic force microscopy image of kagome lattice $K4$ at remanence. The kagome lattice was saturated in a magnetic field at the orientation $\phi=0°$ before the microscopy. The small arrows show the direction of the magnetization vector for some representative islands.

show no appreciable change, as compared to the $\phi=0°$ orientation. Due to higher order effects in the MOKE signal, the measured hysteresis curve $0x$ shows a peak at $H=100$ Oe. However, the hysteresis curves measured at the first diffraction spot ($1x$ and $1y$) indicate a very different reversal process compared to the previous one, which is dominated by domain formation and propagation instead of coherent rotation. Here, the true strength of the Bragg MOKE technique becomes evident. The different processes are not visible in specular reflectivity measurements; they become obvious only in the higher order Fourier components. In the first part of the reversal process, the calculated magnetization rotates inside the particles of sublattices $S1$ and $S3$ toward the easy axis direction, as expected. At remanence, sublattice $S2$

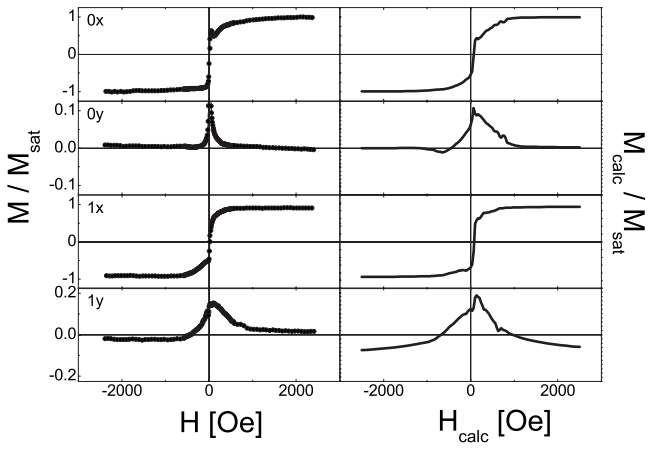

FIG. 14. Kagome lattice $K1$: Measured (left panel) and calculated Bragg MOKE hysteresis loops (right panel) for the x and y components at the diffraction spots for $\phi=30°$; only the ascending branches of the hysteresis loops are shown.

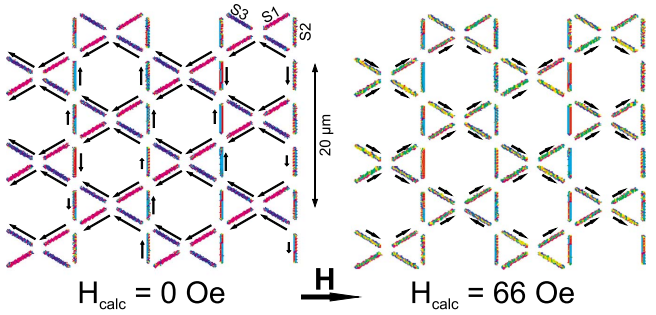

FIG. 15. (Color online) Kagome lattice $K1$: Calculated magnetization distribution in the three sublattices $S1$, $S2$, and $S3$. The left panel is calculated for an external field $H_{calc}=0$, the right panel for a field $H_{calc}=66$ Oe oriented perpendicular to the sublattice $S2$, which is referred to as the orientation $\phi=30°$. The arrows indicate the net magnetization direction inside the rectangular islands.

shows indeed both up and down orientations, and in some cases a domain state. Thus, at $H_{calc}=0$ Oe, sublattices $S1$ and $S3$ are parallel or ferromagnetically aligned, whereas sublattice $S2$ is disordered. With increasing positive field, domain formation takes place in all three sublattices (see Fig. 15, $H_{calc}=66$ Oe). At $H_{calc}=166$ Oe, the magnetization reversal of $S1$ and $S3$ via domain formation is completed (calculated magnetization distribution not shown for this field value). In the calculated hysteresis curve $1y$, the magnetization reaches its local minimum value. The remagnetization of sublattice $S2$ continues until $H_{calc}=900$ Oe. At this point, the calculated hysteresis curves $0y$ and $1x$ reach the saturation magnetization.

Here, we would like to point out that in some cases, it is not possible to reach an adequate agreement between measurement and simulation, as can be seen for the hysteresis curve $0y$ in Fig. 14. The shape of the simulated hysteresis curve agrees more or less with the measured one, but the magnetic fields differ very strongly: in the simulation, the peak at the coercive field is much broader than in the measurement. As we have made some restrictions to the cell size in the simulations, which affect the remagnetization process, and as we have taken the complex higher order effects in the

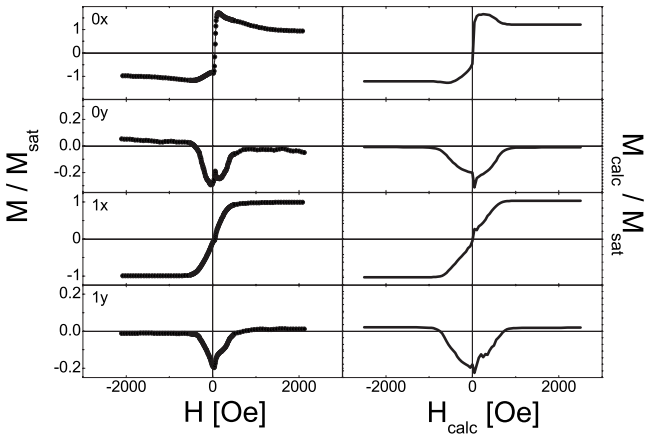

FIG. 16. Measured (left panel) and calculated Bragg MOKE hysteresis loops (right panel) similar to Fig. 14 but for kagome lattice $K2$.

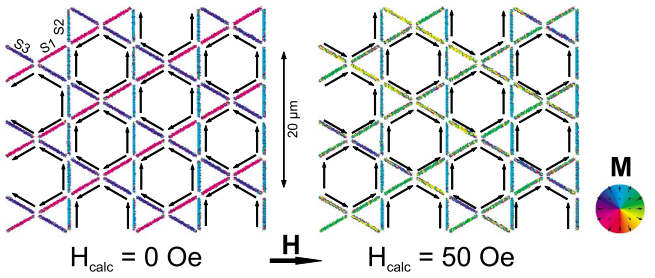

FIG. 17. (Color online) Calculated magnetization distribution similar to Fig. 15 but for kagome lattice $K2$.

MOKE signal into account, this is not too surprising. Nevertheless, if the Bragg MOKE curves of order $n>0$ agree to each other, we regard the simulations as reliable.

2. Vector magneto-optical Kerr effect results, K2

The reversal process of lattice $K2$ also begins with the rotation of the magnetization vectors inside the bars, which can easily be seen in the measured hysteresis curves depicted in Fig. 16. Like in $K1$, the measured hysteresis curve of $0x$ is affected by higher order effects resulting in overshoots higher than saturation. This behavior has been taken into account for the calculated hysteresis curve. All four curves show a nucleation field of $H_N=-440$ Oe. In the simulated curves, the nucleation field is $H_N=-700$ Oe. In contrast to lattice $K1$, the magnetization in sublattice $S2$ is not as strongly affected by domain formation in the remanent state (see Fig. 17). The stray field at positions A and B where $S2$ crosses the other two sublattices is clearly larger here than in lattice $K1$ due to the smaller distance b (see Table IV). The stronger magnetostatic coupling in sublattice $S2$ prevents domain formation. This leads to three ordered sublattices in the remanent state. However, unlike for the $\phi=0°$ orientation, here, the triangles do not form a flux closure state. The calculated curves are qualitatively similar to the experimental ones. At remanence, we notice an overshoot in the $0x$ component, which is higher than the saturation value. As this is unphysical, second-order effects must play a role. This is confirmed by the simulation of the $0x$ component, where the second-order effect has explicitly been taken into account. At $H_{calc}=50$ Oe, the net magnetization inside the rectangles of sublattices $S1$ and $S3$ reverses, but domains still exist. The

TABLE IV. Stray field H_{stray} obtained from the micromagnetic simulations at remanence for $\phi=0°$. For further explanation, we refer to the text.

Lattice	b (μm)	H_{stray} (Oe) Position A	Position B	Position C
$K1$	1.9	23	29	42
$K2$	1.0	113	99	220
$K3$	1.1	44	51	80
$K4$	0.65	485	78	85

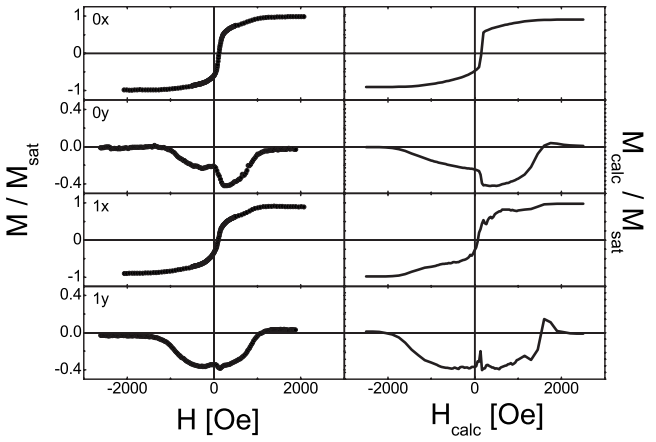

FIG. 18. Measured (left panel) and calculated Bragg MOKE hysteresis loops (right panel) similar to Fig. 14 but for kagome lattice $K3$.

remagnetization process is complete at a field of $H_{calc}=750$ Oe in good agreement with the measured saturation field of about $H=650$ Oe.

3. Vector magneto-optical Kerr effect results, K3 and K4

The magnetization reversal in lattices $K3$ and $K4$ is qualitatively similar to the one in $K2$. However, the tendency of domain formation in the frustrated sublattice $S2$ is larger in $K3$ and $K4$ than in $K2$. For reference, the measured and simulated MOKE hysteresis curves are depicted in Fig. 18 for $K3$ and Fig. 19 for $K4$. The corresponding calculated profiles at remanence and just above coercivity are shown in Figs. 20 and in Fig. 21, respectively.

The calculated hysteresis curves of the three sublattices are depicted in Fig. 22 for all four kagome lattices. As expected, the hysteresis curves of sublattices $S1$ and $S3$ are degenerate because of their orientation with respect to the applied field. The hysteresis curve of sublattice $S2$ is different because the Fe bars on this sublattice are oriented in the hard axis direction with respect to the magnetic field. The

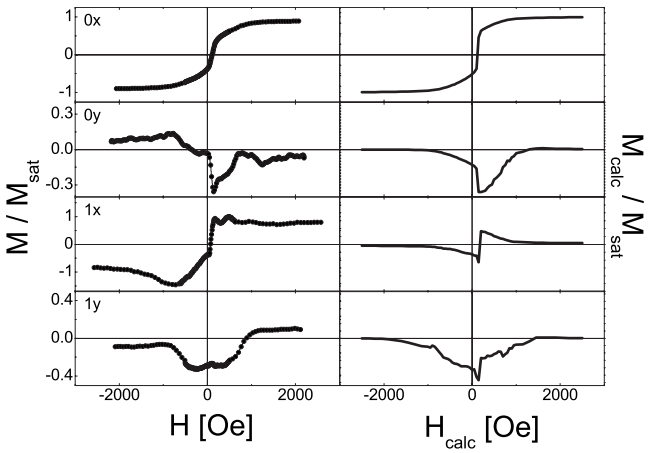

FIG. 19. Measured (left panel) and calculated Bragg MOKE hysteresis loops (right panel) similar to Fig. 14 but for kagome lattice $K4$.

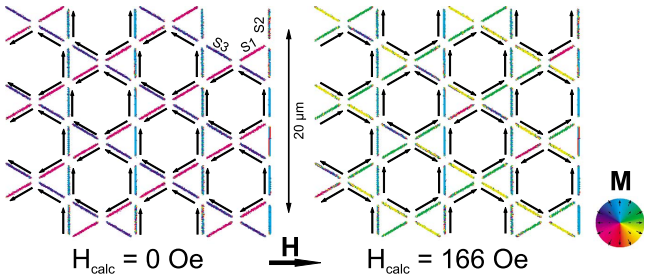

FIG. 20. (Color online) Calculated magnetization distribution similar to Fig. 15 but for kagome lattice *K*3.

four kagome structures differ only in their coercive fields and the remanent magnetization as listed in Table V. The measured coercive fields show the same tendency as for the $\phi = 0°$ orientation (see Table III). The coercive field of *K*3 is the largest one, followed by the coercive field of *K*4, whichis larger than those of *K*1 and *K*2. Except for *K*1, experiment and simulation are in good agreement. The measured values of the remanent magnetization are also in good agreement with the simulated results. Because of the strong second-order MOKE contributions in the hysteresis of structure *K*2, no reliable value for remanence can be provided. The second-order contributions may also affect the coercive field of the hysteresis curves. Note that the calculated 0*x* hysteresis curves of *K*1 and *K*2 shown in Fig. 22 do not take second-order effects into account, as observed in the experimental hysteresis curves, whereas the calculated 0*x* curves in Figs. 14 and 16 include second-order effects.

4. Magnetic force microscopy and x-ray photoemission electron microscopy images

MFM images in the remanent state of all four kagome lattices are depicted in Fig. 23. The poles of the magnetization can clearly be seen at the ends of the rectangles. However, as the contrast has been optimized for each single picture, a quantitative comparison between the MFM images and the calculated stray fields is not possible. Nevertheless, some qualitative features are clearly visible. In *K*2 and *K*4, it can be seen that the stray fields are higher for positions *A* and *C* than for *B*. In position *B*, the stray fields appear to be compensated. In *K*3, all three vertices can be recognized in the MFM image, in agreement with the more equal stray fields predicted by the simulation (see Table IV). The *K*1 image is the most difficult one to interpret, most likely due to

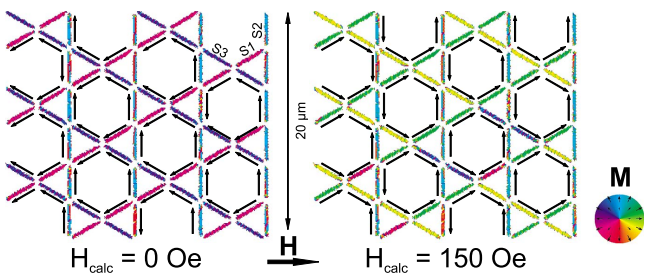

FIG. 21. (Color online) Calculated magnetization distribution similar to Fig. 15 but for kagome lattice *K*4.

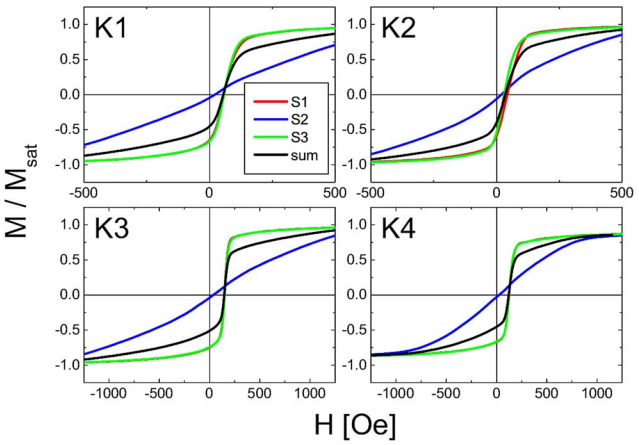

FIG. 22. (Color online) Hysteresis loops 0*x* of each sublattice *S*1 (red), *S*2 (blue), and *S*3 (green) obtained from the simulations of the four kagome structures. The black line corresponds to the sum hysteresis loop.

the very low stray fields expected for all three vertices.

The resolution of MFM is not high enough to observe and analyze the inner domain structure within the rectangular bars. Therefore, we used X-PEEM with a higher resolution on the 50 nm scale to record the inner magnetic structure.[34] X-PEEM images for the kagome lattices *K*3 and *K*4 in the remanent state are depicted in Fig. 24, after they have been exposed to a saturation field. The contrast in gray scale corresponds to the projection of the magnetization vector onto the vertical axis, i.e., only information of the magnetization component m_y can be inferred from the images. The images clearly show the different magnetization directions in each sublattice. The image of *K*3 confirms that the magnetization inside sublattices *S*1 and *S*3 is more or less uniform. In some of the bars, the magnetization has already reversed its direction. The domain formation in sublattice *S*2 is much stronger. As sublattice *S*2 is oriented in the hard axis direction and because of the magnetization direction in the two other sublattices, the magnetization is frustrated in *S*2 and, therefore, easily breaks up into domains. The strong coupling between single elements leads to mirror domains at the end of the bars. The micromagnetic simulation of the remanent state with a finer cell size of 25 nm in Fig. 25 confirms the appearance of such mirror domains.

The magnetization configuration in structure *K*4 is imaged at the edge of the pattern. The images show that the magne-

TABLE V. Coercive field and remanence obtained from the measurements and the micromagnetic simulations for $\phi = 30°$.

	Experiment		Simulation	
Lattice	H_c (Oe)	$\theta_K^{rem}/\theta_K^{sat}$	$H_{calc,c}$ (Oe)	Remanent/saturated
*K*1	12	0.45	55	0.45
*K*2	55		36	0.40
*K*3	111	0.62	145	0.51
*K*4	104	0.42	119	0.45

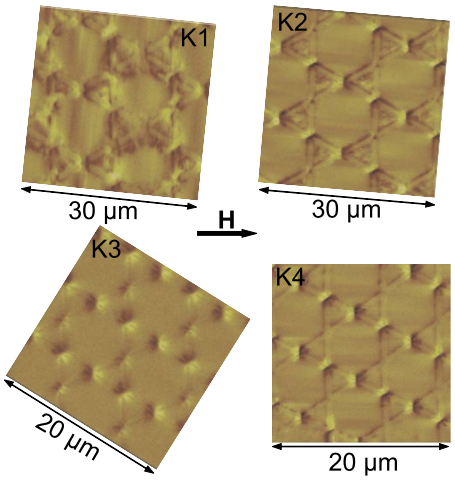

FIG. 23. (Color online) Magnetic force microscopy images of all four kagome lattices in remanence. The kagome lattices were first saturated in a magnetic field at the orientation $\phi=30°$ as indicated, before taking the microscopy images.

tization in sublattice $S1$ is already reversed with respect to $S3$. This behavior is in conflict with the calculated magnetization profiles and with the MFM pictures and may be explained by the fact that the magnetostatic coupling at the rim of the pattern is different from the center.

IV. DISCUSSION AND CONCLUSION

The vector and Bragg MOKE data together with the micromagnetic simulations on arrays with kagome symmetry show a very interesting general tendency. While at remanence the four lattices show almost identical behavior, the magnetization reversal of lattice $K1$ differs from that of $K2-K4$. Especially intriguing is the magnetization switching in samples of orientation $\phi=0°$. In all four lattices, switching from the left- to the right-oriented onion state (see, e.g., Fig. 5, left) via an intermediate configuration (see, e.g., Fig. 5, right) occurs. However, this intermediate configuration for $K1$ is different from those of $K2-K4$. In the first case ($K1$), it consists of sublattices $S2$ and $S3$ oriented along the external field and $S1$ opposite to it (Fig. 5), i.e., sublattices $S2$ and

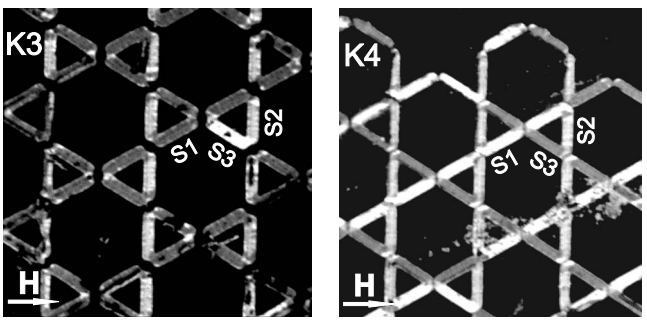

FIG. 24. Photoemission electron microscopy image of kagome lattices $K3$ and $K4$ in remanence. The kagome lattices were saturated in a magnetic field at the orientation $\phi=30°$ as indicated, before taking the microscopy picture in remanence.

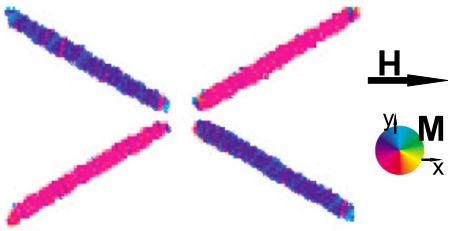

FIG. 25. (Color online) Magnetization distribution of kagome lattice $K3$ for sample orientation $\phi=30°$, showing the remanent state. The simulation was performed with a cell size of 25 nm.

$S3$ rotate first (switching path $S2S3$). In all other lattices, $\vec{S1}\|\vec{H}$, while $S2$ and $S3$ have components antiparallel to the field (Fig. 11), i.e., the intermediate configuration is reached by the rotation of sublattice $S1$ (switching path $S1$). Additionally, the coercive field of the switching increases for lattices $K2-K4$ with respect to that of lattice $K1$. In the following, we will discuss the reasons for different magnetization reversals.

All four arrays have identical symmetry and material properties with different interparticle distances and particle aspect ratios. The shape of a particle has an influence on the magnetization reversal of each individual element as well as magnetostatic interactions and, hence, a collective behavior of an array.[20,35] To understand the puzzling magnetization reversal, we have calculated the strength of magnetostatic moments and interactions in the kagome ensembles.[36] Our calculations show that lattice $K1$ can be approximated as a pure dipolar ensemble with dipole strength $|Q_{10}^{K1}|=1.35\times10^{-14}\,\mathrm{m}^2$, while in all other cases, the octopolar contributions are strong $(1/2|Q_{10}|)$ and have to be taken into account.

In the next step, we calculate the magnetostatic energies per particle for the onion E_{on}^{K1}, E_{on}^{K2-K4} and the intermediate

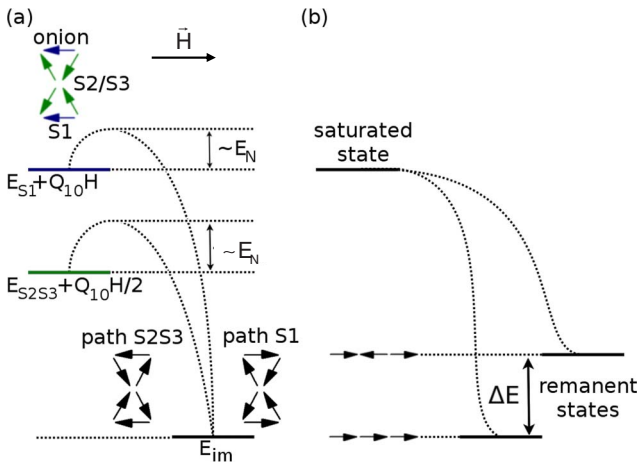

FIG. 26. (Color online) (a) Magnetostatic energy of sublattices $S1$ (blue) and $S2$, $S3$ (green) for the sample orientation $\phi=0°$. The energy levels of the onion state (upper inset) are shown on the left of the intermediate state (bottom insets) E_{im} on the right hand side. The dashed lines schematically show the nucleation energy barriers. (b) Magnetostatic energy levels for the saturated and two possible remanent states at sample orientation $\phi=30°$. Arrows indicate the direction of magnetization in sublattice $S2$.

states E_{im}^{K1}, E_{im}^{K2-K4} shown in the right inset of Fig. 5 and the left inset of Fig. 11. There exist two variations of the intermediate configuration differing by the twist of the magnetization in the triangles [see also the inset in Fig. 26(a)]. The magnetostatic energies of left hand and right hand intermediate states are degenerate $E_{im}^{K1}=-2.3d$ and $E_{im}^{K2-K4}=-3.1d$, where d is the dipole-dipole interaction energy between two mutually parallel and perpendicular to the connection line moments at the nearest neighbor distance of corresponding array. The magnetostatic energy of the onion pattern is not homogeneous. Unlike the intermediate configuration having identical energy for any particle, there exist two energy levels in the onion state. The moments belonging to sublattices $S2$ and $S3$ occupy the lower energy level ($E_{S2S3}^{K1}=-0.6d$, $E_{S2S3}^{K2-K4}=-0.8d$), while those of $S1$ the higher energy level ($E_{S1}^{K1}=+1.1d$, $E_{S1}^{K2-K4}=+1.5d$) [see Fig. 26(a)]. All energy levels of onion states lie higher than those of the intermediate ones. Hence, it is not surprising that the remagnetization occurs via those degenerated states.

As sublattice $S1$ has larger magnetostatic energy, the energy gain after the magnetization reversal for $S1$ is larger than that of sublattices $S2$ and $S3$. On the other hand, the magnetic moments of $S1$ are antiparallel to the applied field, i.e., the field exerts no torque on sublattice $S1$, while sublattices $S2$ and $S3$ are subjected to the torque with the corresponding energy contribution $E_\tau=\int \tau d\phi=Q_{10}H/2$. Thus, during the reversal via path $S2S3$, sublattices $S2$ and $S3$ gain less energy but the magnetic torque helps to do this. This subtle interplay between static and dynamic magnetic phenomena determines the way of magnetization reversal.

The decisive role for the choice of a remagnetization path plays the energy of domain nucleation in the magnetic particles. It has been experimentally established that in Fe elements, magnetization reverses via domain formation. Magnetization reversal in such a case is mainly determined by the domain nucleation energy. This energy is different for weaker coupled lattice $K1$ and stronger interactions $K,\ldots,K4$. In the first case ($K1$), the domain nucleation energy E_N can be estimated by $E_N=\Omega\sqrt{AK}\approx 3.6\times 10^{-17}$ J, where Ω is the area of a domain wall, $A=21\times 10^{-12}$J/m is the exchange stiffness, and $K=\mu_0 M_s^2/2=1.7,\ldots,1.9\times 10^6$ J/m^3 is the shape anisotropy energy density.[37] This value corresponds to field of 26.5 Oe, which is in good agreement with the experimentally found 30 Oe for lattice $K1$.

In more densely packed lattices $K2-K4$, the strong octopolar contributions stabilize an initial magnetization direction in sublattice $S1$ and additional nucleation energy has to be paid for the magnetization reversal.[35] As can be seen from Table II, the required E_N corresponds to the field of >200 Oe. However, already smaller fields are sufficient to exert significant torque on the magnetization of sublattices $S2$ and $S3$. Therefore, in denser packed arrays $K2,\ldots,K4$, sublattices $S2$ and $S3$ switch before the nucleation of domains in sublattice $S1$.

For samples oriented at 30° with respect to the field, the magnetization reversal is very similar in all four structures $K1-K4$. The main difference between $K1$ and the other structures lies in the behavior of sublattice $S2$. Generally, at remanence, the magnetization of sublattice $S2$ forms parallel lines of magnetic moments, which are oriented perpendicular to the field. While in the dense packed lattices $K2-K4$ there are almost no exceptions, the lattice structure $K1$ shows a very pronounced domain formation as well as some misaligned particles at $H\approx 200$ Oe (see Fig. 15).

The schematic representation of the magnetostatic energy levels for this case is given in Fig. 26(b). On the left, the energy of the saturated magnetic configuration is depicted. On the right, the energy levels of remanent states with two possible arrangements of nett magnetic moments in sublattice $S2$ are shown. In contrast to the case of $\phi=0°$ sample orientation, there are no energy barriers for the magnetization reversal, as in saturation, all Fe elements are magnetized along their hard axis. As one can easily recognize from the diagram in Fig. 26(b), the configuration with parallel $S2$ lines has lower energy. However, the energy difference between two possible remanent states ΔE for weaker coupled lattice $K1$ is small, while it increases with increasing octopolar contribution $\Delta E_{K2-K4}/\Delta E_{K1}\approx 1.5$. This explains the preference of parallel alignment of elements $S2$ in dense lattices $K2-K4$ and their stability in the applied magnetic field.

To conclude, we have investigated by a combination of Bragg MOKE and vector MOKE the magnetization reversal of Fe rectangular islands, which are placed between the vertices of a kagome lattice. The aspect ratio of the islands was chosen such that they dominantly form a macroscopic magnetic moment at remanence. These moments are allowed to interact via their magnetic stray fields with their neighbors placed at different distances. The Fe bars on the kagome pattern can be subdivided into three sublattices with triangular symmetry. The magnetization reversal was investigated by applying a magnetic field either parallel to one of the sublattices (0° orientation) or perpendicular to one sublattice (30° orientation). To complete the analysis, micromagnetic simulations with the OOMMF package were performed for calculating the magnetization distribution within the kagome pattern and for calculating the MOKE response. Furthermore, MFM and PEEM images were taken to image the net macroscopic magnetization pattern of a whole array and the domain structures within each individual particle in the remanent state. For the 0° orientation, we discovered two reversal processes. In case that the interaction between the net magnetic moments is weak, the particles inclined to the field direction by 60° flip first, followed by the sublattice parallel to the applied field. For stronger interaction at reduced particle distance, the parallel sublattice switches first, followed by the domain process in the inclined bars. Applying a magnetic field in the 30° orientation automatically leads to a strong frustration of the particles with the hard axis orientation. This frustration causes domain formation preferentially in the perpendicular bars. We have analyzed the magnetostatic interaction in the pattern and found that higher order terms strongly influence the magnetization reversal in densely packed magnetic arrays with kagomé symmetry. The effect of the multipolar moments is twofold. First, it influences the collective magnetic ordering in an array, and second, it changes the nucleation fields due to the stabilization of magnetization near the edges of neighboring magnetic particles.

ACKNOWLEDGMENTS

We would like to thank P. Stauche for the help in sample preparation with the ion-beam-sputtering machine as well as E. Amaladass and A. Scholl for their support during the PEEM measurements at the Advanced Light Source, which is supported by the Director, Office of Basic Energy Sciences, of the U.S. Department of Energy under Contract No. DE-AC02-05CH11231. This work was supported by SFB 491 "Magnetic Heterostructures: Spin Structures and Spin Transport" and SFB 668 "Magnetism from single atom to nanostructure" (A11 and B3) of the Deutsche Forschungsgemeinschaft, which is gratefully acknowledged.

*Corresponding author; hartmut.zabel@ruhr-uni-bochum.de; URL: www.ep4.ruhr-uni-bochum.de

[1] M. Mekata, Phys. Today **56**(2), 12 (2003).
[2] M. Takano, T. Shinjo, M. Kiyama, and T. Takada, J. Phys. Soc. Jpn. **25**, 902 (1968).
[3] M. Wolf and K. D. Schotte, J. Phys. A **21**, 2195 (1988).
[4] D. S. Greywall and P. A. Busch, Phys. Rev. Lett. **62**, 1868 (1989).
[5] M. Nishiyama, S. Maegawa, T. Inami, and Y. Oka, Phys. Rev. B **67**, 224435 (2003).
[6] D. Grohol, K. Matan, J.-H. Cho, S.-H. Lee, J. W. Lynn, D. G. Nocera, and Y. S. Lee, Nat. Mater. **4**, 323 (2005).
[7] K. Matan, D. Grohol, D. G. Nocera, T. Yildirim, A. B. Harris, S.-H. Lee, S. E. Nagler, and Y. S. Lee, Phys. Rev. Lett. **96**, 247201 (2006).
[8] V. Elser, Phys. Rev. Lett. **62**, 2405 (1989).
[9] J. Atwood, Nat. Mater. **1**, 91 (2002).
[10] J. I. Martín, J. Nogués, K. Liu, J. L. Vicent, and I. K. Schuller, J. Magn. Magn. Mater. **256**, 449 (2003).
[11] R. P. Cowburn, Phys. Rev. B **65**, 092409 (2002).
[12] R. E. Dunin-Borkowskia, M. R. McCartney, B. Kardynal, and D. J. Smith, J. Appl. Phys. **84**, 374 (1998).
[13] V. Novosad, K. Yu. Guslienko, H. Shima, Y. Otani, S. G. Kim, K. Fukamichi, N. Kikuchi, O. Kitakami, and Y. Shimada, Phys. Rev. B **65**, 060402(R) (2002).
[14] R. Wang, C. Nisoli, R. S. Freitas, J. Li, W. McConville, B. Cooley, M. S. Lund, N. Samarth, C. Leighton, V. H. Crespi, and P. Schiffer, Nature (London) **439**, 303 (2006).
[15] A. Remhof, A. Schumann, A. Westphalen, H. Zabel, T. Last, U. Kunze, N. Mikuszeit, and E. Y. Vedmedenko, Phys. Rev. B **77**, 134409 (2008).
[16] Y. Tabata, H. Kadowaki, K. Matsuhira, Z. Hiroi, N. Aso, E. Ressouche, and B. Fak, Phys. Rev. Lett. **97**, 257205 (2006).
[17] A. A. Fraerman and M. V. Sapozhnikov, Phys. Rev. B **65**, 184433 (2002).
[18] Y. Takagaki and K. H. Ploog, Phys. Rev. B **71**, 184439 (2005).
[19] D. Suess, T. Schrefl, J. Fidler, and V. Tsiantos, IEEE Trans. Magn. **37**, 1960 (2001).
[20] E. Y. Vedmedenko, N. Mikuszeit, H. P. Oepen, and R. Wiesendanger, Phys. Rev. Lett. **95**, 207202 (2005).
[21] P. Vavassori, M. Grimsditch, V. Novosad, V. Metlushko, and B. Illic, Phys. Rev. B **67**, 134429 (2003).
[22] T. Schmitte, K. Theis-Bröhl, V. Leiner, H. Zabel, S. Kirsch, and A. Carl, J. Phys.: Condens. Matter **14**, 7525 (2002).
[23] A. Westphalen, K. Theis-Bröhl, H. Zabel, K. Rott, and H. Brückl, J. Magn. Magn. Mater. **302**, 181 (2006).
[24] Th. Zeidler, F. Schreiber, H. Zabel, W. Donner, and N. Metoki, Phys. Rev. B **53**, 3256 (1996).
[25] A. Westphalen, M.-S. Lee, A. Remhof, and H. Zabel, Rev. Sci. Instrum. **78**, 121301 (2007).
[26] C. Daboo, R. J. Hicken, E. Gu, M. Gester, S. J. Gray, D. E. P. Eley, E. Ahmad, J. A. C. Bland, R. Ploessl, and J. N. Chapman, Phys. Rev. B **51**, 15964 (1995).
[27] M. Grimsditch and P. Vavassori, J. Phys.: Condens. Matter **16**, R275 (2004).
[28] A. Westphalen, A. Schumann, A. Remhof, H. Zabel, T. Last, and U. Kunze, Phys. Rev. B **74**, 104417 (2006).
[29] R. M. Osgood, B. M. Clemens, and R. L. White, Phys. Rev. B **55**, 8990 (1997).
[30] R. M. Osgood III, S. D. Bader, B. M. Clemens, R. L. White, and H. Matsuyama, J. Magn. Magn. Mater. **182**, 297 (1998).
[31] S. Yan, R. Schreiber, P. Grünberg, and R. Schäfer, J. Magn. Magn. Mater. **210**, 309 (2000).
[32] M. J. Donahue and D. G. Porter, National Institute of Standards, Technology Interagency Report No. NISTIR 6376, 1999 (unpublished).
[33] J. Rothman, M. Kläui, L. Lopez-Diaz, C. A. F. Vaz, A. Bleloch, J. A. C. Bland, Z. Cui, and R. Speaks, Phys. Rev. Lett. **86**, 1098 (2001).
[34] T. Eimüller, T. Kato, T. Mizuno, S. Tsunashima, C. Quitmann, T. Ramsvik, S. Iwata, and G. Schütz, Appl. Phys. Lett. **85**, 2310 (2004).
[35] E. Y. Vedmedenko, Phys. Status Solidi B **244**, 1133 (2007).
[36] N. Mikuszeit, E. Y. Vedmedenko, and H. P. Oepen, J. Phys.: Condens. Matter **16**, 9037 (2004).
[37] R. C. O'Handley, *Modern Magnetic Materials* (Wiley, New York, 2000).